MDPI

Article

Seismic Performance Evaluation of a Frame System Strengthened with External Self-Centering Components

Yulin Fan [1], Jiaye Song [1], Xuelu Zhou [1] and Hang Liu [2],*

[1] School of Civil and Transportation Engineering, Beijing University of Civil Engineering and Architecture, Beijing 100044, China; m18511431998@163.com (Y.F.); songjiaye0123@163.com (J.S.); zhouxuelu1@163.com (X.Z.)

[2] Beijing Building Construction Research Institute Co., Ltd., Beijing 100039, China

* Correspondence: liuhang71@163.com

Abstract: In the context of China's promotion of green buildings and resilient urban development, new reinforcement technologies offer significant development prospects, while traditional methods have limited effectiveness in enhancing structural resilience. To address this latter issue, this study proposes a novel reinforcement method that involves enlarging the structural cross-section and adding external self-resetting components to improve seismic performance. While this method has been validated through quasi-static tests, limitations in terms of sample size and experimental conditions necessitate further research into the seismic performance and dynamic behavior of the reinforced framework. Consequently, this study uses finite element analysis to explore the influencing factors and dynamic characteristics of the reinforcement method. The results show that finite element modeling effectively simulates the stress characteristics of reinforced frameworks. Installing prefabricated beams significantly enhances the load-bearing capacity by 18% and reduces the residual deformation rates after earthquakes by 26%. Increased pre-tensioning of the steel strands further improves seismic resilience. This reinforcement method enables older structures lacking self-resetting capabilities to achieve some degree of self-resetting ability, and it performs well under various earthquake conditions.

Keywords: seismic reinforcement; self-centering; finite element analysis; time-history analysis

1. Introduction

In 2021, the accumulated floor area of existing buildings in China was 80 billion m^2. Of this area, only 6.5 billion m^2 met current green building standards, and the accumulated total floor area has been increasing annually by 2 billion m^2. Moreover, the seismic resistance of many buildings exceeding their design and service lives does not meet current requirements. Additionally, structural changes due to industrial transformation necessitate the re-planning and retrofitting of existing buildings to ensure their safety, especially regarding seismic performance.

For general buildings, seismic retrofitting primarily aims to enhance their resilience to meet the requirement of experiencing "minor damage from small earthquakes, repairable damage from moderate earthquakes, and no collapse from major earthquakes". With rapid urban development, performance-based design methods are crucial for retrofitting existing buildings, as well as for assessing current structural seismic performance standards. Previous studies [1–6] have extensively discussed performance-based retrofitting methods, focusing on three types of performance targets.

In this study, an existing building in Beijing was selected for retrofitting research. Due to its age, inadequate seismic performance, and reduced structural capacity as a result of interior renovations, it was determined that the targeted retrofitting of this building was necessary. Traditional methods for reinforced-concrete frame structures include section enlargement [7–9], externally bonded steel reinforcement [10], external prestressing, carbon

fiber wrapping [11–16], the addition of shear walls [17], and the addition of supports [18,19]. One particularly novel retrofitting system, the self-centering mechanism, has been thoroughly explored in previous research [20–24]. By combining traditional methods with this self-centering system, this paper proposes a retrofitting approach based on using externally attached self-centering components to retrofit selected frames. This displacement-based retrofitting process begins with section enlargement to significantly improve the load-bearing capacity and lateral resistance. Subsequently, prefabricated beams are externally attached to one side of the enlarged sections [25,26], utilizing the elastic tightening effect of the steel tendons to restore the retrofitted frame to its original position post-earthquake, thereby reducing residual deformations and providing the additions with a self-centering capability. The resetting mechanism of the reinforced frame is shown in Figure S1.

Although this retrofitting technology has been validated through quasi-static tests on scaled-down frame models, the limited number of samples and potential data acquisition errors necessitate further evaluation of the seismic performance of buildings after retrofitting using this method. This study combined finite element analysis with ABAQUS (V6.14) [27–31] and OpenSees (V3.0.3) [32–37] software, comparing the numerical simulation results with quasi-static test results to verify the accuracy and rationality of the modeling methods. Additionally, parameter sensitivity analysis using ABAQUS was conducted to investigate the impact of steel cable prestressing and energy dissipation on the overall seismic performance of the frame. OpenSees (V3.0.3) was used to investigate the seismic performance of the reinforced frame under different earthquake wave inputs and to evaluate the dynamic characteristics of the reinforced structure.

2. Parameter Variation Simulation Using ABAQUS

2.1. Test Model Description

The simulation experiments were based on quasi-static test data from existing retrofitted frames with externally attached self-centering components. The test utilized an existing prototype building in Beijing's Dongcheng District; due to its old design, this building was assessed in 2017 by relevant agencies and found to be inadequate in terms of its structural and seismic performance based on current standards. Therefore, an approach using externally attached self-centering components was designed for retrofitting. The experiment involved three scaled-down models (denoted as LF1, LF2, and LF3, as shown in Table 1), and low-cycle reciprocating loading tests were conducted at the Vibrations Laboratory of Beijing University of Civil Engineering and Architecture. The loading regime for the three frames is shown in Figure S2. The dimensions of the original and reinforced frames are shown in Figure 1.

Table 1. Parameters of the test specimens.

Specimen ID	Concrete (Unreinforced/Reinforced)	Column Section (mm)	Beam Section (mm)	d_e [1] (mm)	Prestressed Steel Tendons	$\sigma_{pe}{}^t A_p$ [2] (kN)
LF1	C20/-	270×270	150×306	--	--	--
LF2	C20/Grouting material	390×480	270×426	14	2Ø15.2	51.3
LF3	C20/Grouting material	390×480	270×426	20	4Ø15.2	43.0

[1] The diameter of the energy-dissipating steel rebar is denoted as d_e. [2] The measured effective prestress of a single prestressed tendon is denoted as $\sigma_{pe}{}^t A_p$.

2.2. Establishment of ABAQUS Model

Table 2 shows the ABAQUS model conditions. Through simulation, three sets of finite element models were fitted and compared with experimental data to validate the correctness of the finite element model setup. Additionally, to study the effect of the externally attached self-centering components on the frames reinforced only through section enlargement, model EM was established.
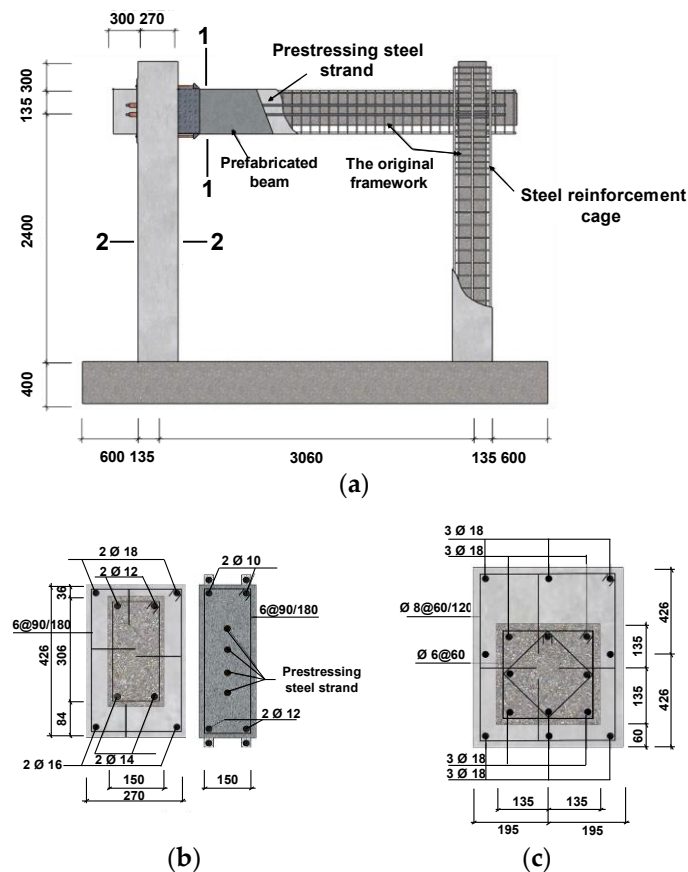
Figure 1. Test systems for the retrofitted concrete frames using self-centering components (the dimensions in the figure are in mm). (**a**) Photographs of the experimental site. (**b**) Section 1-1: Dimensions of the reinforced frame beams. (**c**) Section 2-2: Dimensions of the reinforced frame columns.

The simulated frames S1, S2, and S3 were designed based on the dimensions of frames LF1, LF2, and LF3 from the static tests. Before reinforcement, the dimensions of the column in frame S1 were 270 × 270 mm, and the beam dimensions were 105 × 306 mm. After reinforcement, the dimensions of the column in frame S2 increased to 390 × 480 mm, with beam dimensions of 270 × 426 mm. This frame also featured prefabricated beams measuring 150 × 426 mm, and they were internally tensioned with two unbonded prestressed tendons. For frame S3, after reinforcement, the column dimensions were 390 × 480 mm, the beam dimensions were 270 × 426 mm, and the prefabricated beams measured 150 × 426 mm; however, they were also internally tensioned with four unbonded prestressed tendons. All longitudinal reinforcements for the columns and beams in the models were HPB400-grade steel bars, while the hoop reinforcements were HRB300-grade steel bars. The prestressed tendons were all 15.2 mm in diameter and made of 1860-grade steel strands.

To investigate the combined effect of the prestressed tendon force on the frame's bearing capacity and the residual deformation under horizontal loading, frames P80 and P120 were established using Frame S2 as a reference with varied parameters. In addition, to study the influence of the energy-dissipating steel rebar diameter and its constitutive behavior at nodes on the frame's seismic performance, frames ED0, ED20, EM1, and EM2 were established with various parameters, using Frame S2 as a reference.

To simulate the shear slip between the steel reinforcement and concrete in the reinforced-concrete frames before and after strengthening, the "Embed" constraint was used for degree-of-freedom coupling based on the load characteristics. Additionally, to prevent stress concentration at the ends of the concrete columns and beams during loading, 10 mm thick rigid pads were placed at the loading points.

Table 2. ABAQUS finite element modeling experiments.

ABAQUS Simulation Variable Grouping	Specimen ID	Columns		Beam		Energy-Dissipating Steel Bar		Prestressed Steel Tendons	
		Section Dimensions (mm × mm)	Concrete Strength	Section Dimensions (mm × mm)	Concrete Strength	Diameter (mm)	Material	Quantity (*n*)	Effective Prestressing of a Single Steel Tendon (kN)
Experiment simulation	S1	270 × 270	C20	150 × 306	C20	-	-	-	-
	S2	390 × 480	C20/C40	270 × 426	C20/C40	14	Q235	2	40
	S3	390 × 480	C20/C40	270 × 426	C20/C40	14	Q2355	4	40
Section enlargement strengthening	ES	390 × 480	C20/C40	270 × 426	C20/C40	-	-	-	-
Steel strand prestressing	P80	390 × 480	C20/C40	270 × 426	C20/C40	14	Q2355	2	80
	P120	390 × 480	C20/C40	270 × 426	C20/C40	14	Q235	2	120
Diameter of energy-dissipating steel reinforcement	ED0	390 × 480	C20/C40	270 × 426	C20/C40	0	Q235	2	40
	ED20	390 × 480	C20/C40	270 × 426	C20/C40	20	Q235	2	40
Material of energy-dissipating steel reinforcement	EM1	390 × 480	C20/C40	270 × 426	C20/C40	14	HRB335 (400)	2	40
	EM2	390 × 480	C20/C40	270 × 426	C20/C40	14	HRB400 (500)	2	40

To simulate the reinforcement of the frames using the section enlargement method, models S2 and S3 utilized the "Tie" constraint to handle the degrees of freedom at the interface between new and existing concrete. The reinforcement cage and the overall model were coupled using the "Embed" constraint. The "Truss" element was employed to simulate the mechanical behavior of the energy-dissipating steel reinforcements, with 10 mm thick steel pads placed at the ends. Multi-point constraints (MPCs) were used to couple the degrees of freedom across different elements. To model the characteristics of the prestressed tendons, Truss elements were used to simulate the prestressed steel strands. Temperature reduction methods were applied to introduce prestress, with 10 mm thick rigid tensioning pads placed at fixed ends to prevent stress concentration in the concrete at the ends, as shown in Figure 2.
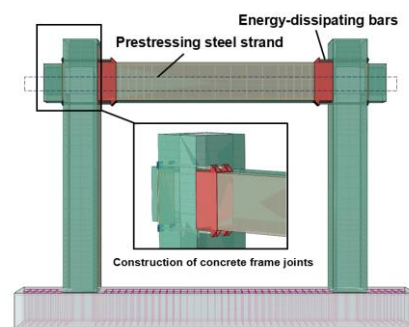
Figure 2. Modeling concrete frame reinforcement with self-centering components in ABAQUS finite element software.

In finite element analysis, the meshing strategy and division of elements are crucial. The mesh density significantly affects the macroscopic concentration effects of plastic damage and softening in concrete elements during loading. Sparse meshing may obscure these effects, while overly dense meshing can lead to non-convergence during computation and errors during the process. In this model, the concrete elements had sizes of 50 mm and the steel reinforcement elements had sizes of 25 mm. From Figure 3a–d, it can be observed that this modeling approach effectively simulated the concrete damage in the reinforced frame. The simulation results closely matched the phenomena observed in the experiments.
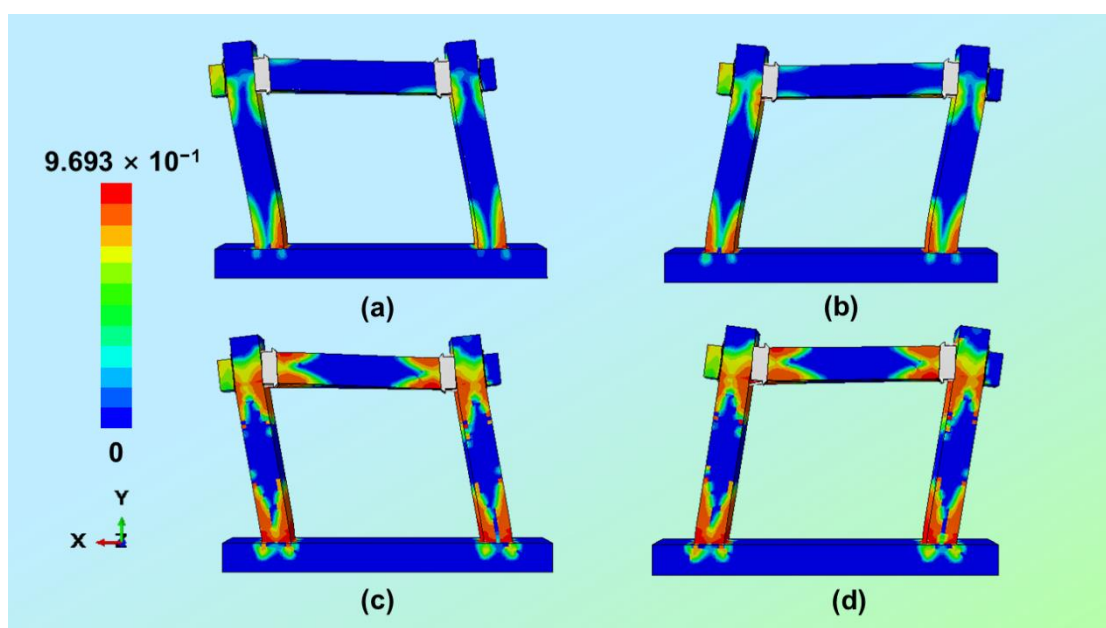
Figure 3. Damage cloud map for reinforced frameworks: (**a**,**b**) cracking load and (**c**,**d**) yield load.

2.3. Calculation Results and Parameter Analysis

A comparison of the displacement–load hysteretic curves obtained from simulations and experiments for three sets of frames is shown in Figure 4. The simulation curves of the three sets of frames generally tracked the corresponding bearing capacities during frame loading quite well. The fitting error of each skeletal curve was <5%. The ascending segments of the simulated hysteretic curves generally matched, while the stiffnesses of the descending segments during unloading were slightly higher than those of the experimental curves. This difference arose because of inherent discrepancies between the constitutive models used in the simulation and those observed in the experiments. In ABAQUS, the simulation of the slip between the steel reinforcement and concrete was less than ideal. However, overall, this modeling approach effectively facilitated the reinforcement of frames with self-resetting components.

Table 3 presents the experimental results of the finite element analysis stages for the simulated frames. From the table, it is evident that increasing the prestress in precast beams could enhance the ductility of the frames strengthened with external self-centering devices. Additionally, the influence of energy-dissipating rebars at nodes on the frame's ductility enhancement was relatively minor.

The energy dissipation curves of each test specimen obtained through ABAQUS simulations are shown in Figure 5. By comparing the frames reinforced only through section enlargement (ES) and specimen S2, it was evident that integrating external prefabricated components enhanced the overall energy dissipation capacity of the frame. Based on the comparison of specimens EM1 and EM2, increasing the material properties of the rebars at the nodes (i.e., increasing the yield strength of the energy-dissipating rebars) did not significantly enhance the overall energy dissipation capacity of the frame. Based on the comparison of specimens ED0 and ED20, increasing the diameters of the energy-dissipating rebars at the nodes notably improved the overall energy dissipation capacity of the frame.

Furthermore, based on the comparison of groups P80 and P120, the increased stress in the prestressed bars within the prefabricated beams, which was facilitated by the tensioning of prestressed steel strands, enhanced the internal frictional energy dissipation significantly, thereby significantly boosting the overall energy dissipation capacity of the frame. In summary, when designing energy-dissipating rebars at nodes, using larger diameters or appropriately increasing the design tension values of the prestressed bars after tensioning can significantly enhance the energy dissipation capacity of the reinforced frames.
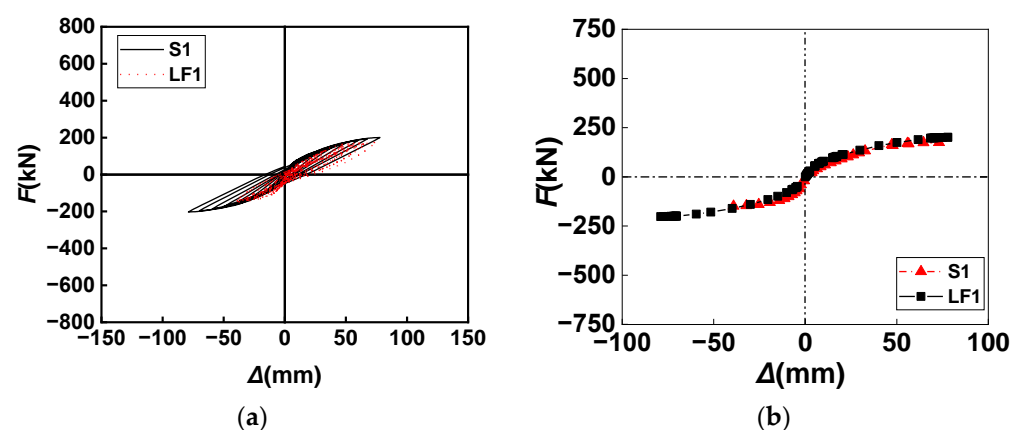
Figure 4. *Cont*.
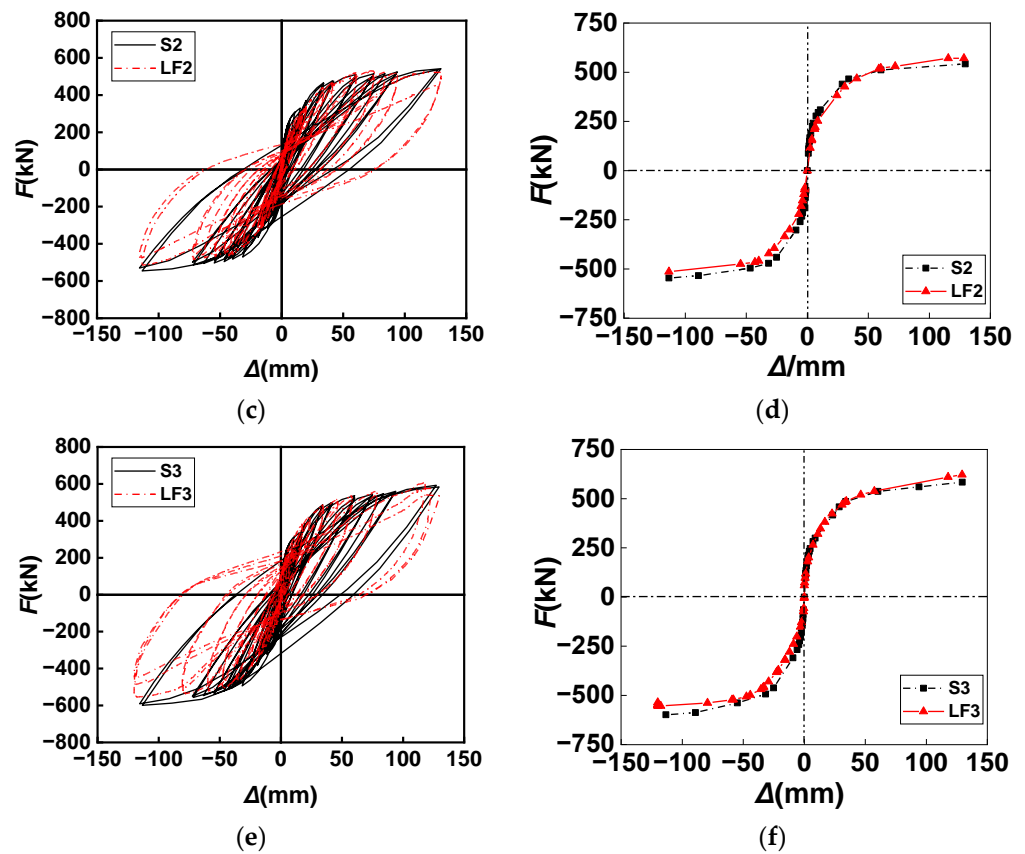
Figure 4. Hysteresis and skeleton curves of quasi-static test and ABAQUS simulation. (**a**) Fitting of the horizontal load–displacement curve for LF1 in ABAQUS. (**b**) Fitting of the skeleton curve for LF1 in ABAQUS. (**c**) Fitting of the horizontal load–displacement curve for LF2 in ABAQUS. (**d**) Fitting of the skeleton curve for LF2 in ABAQUS. (**e**) Fitting of the horizontal load–displacement curve for LF3 in ABAQUS. (**f**) Fitting of the skeleton curve for LF3 in ABAQUS.

Table 3. Experimental results at each main stage of finite element analysis.

Specimen ID	Yield Displacement (mm)	Yield Load (kN)	Ultimate Displacement (mm)	Ultimate Load (kN)	Initial Stiffness (kN/mm)	Ductility Coefficient (μ)
S1	45.23	166.45	97	170.79	12.13	2.16
S2	36.75	417.35	129.479	545.8	94.28	3.52
S3	35.92	417.54	129.479	583.85	103.65	3.6
ES	38.68	386.14	129.479	494.002	89.61	3.34
P80	36.2	417.55	129.479	556.73	101.359	3.57
P120	35.29	418.91	129.479	570.85	104.83	3.66
ED0	36.26	400.35	129.479	542.08	96.77	3.57
ED20	36.1	418.39	129.479	547.04	99.92	3.58
EM1	36.54	417.99	129.479	543.75	98.151	3.54
EM2	36.48	417.87	129.479	543.88	98.151	3.54

Table 4 shows the residual rate simulation results obtained from ABAQUS simulations for each group of specimens. The residual displacement rate *R* can be calculated using the following formula:

$$R = \Delta re / \Delta maX, \tag{1}$$

where Δre represents the residual horizontal displacement of the specimen after the completion of a certain loading level, and Δmax denotes the maximum horizontal displacement during that loading process. It can be observed that the residual deformation rates of all the

specimen groups followed a similar trend as the horizontal loading changed. Comparing the EM frame with other tested frames, it was evident that installing external self-centering devices after reinforcing the frame with section enlargement significantly reduced the residual deformation of the reinforced frame under horizontal load. A comparison of specimens ED0 and ED20 revealed that increasing the diameter of the energy-dissipating rebars did not lead to significant changes in the residual deformation rate of the reinforced frame. Furthermore, the comparison of specimens EM1 and EM2 showed that increasing the material strength of the energy-dissipating rebars at the nodes had no significant impact on reducing the residual deformation of the reinforced frame, while the comparison of specimens P80, P120, and S2 indicated that increasing the prestress in the prefabricated beams effectively reduced the residual deformation of the reinforced frame.
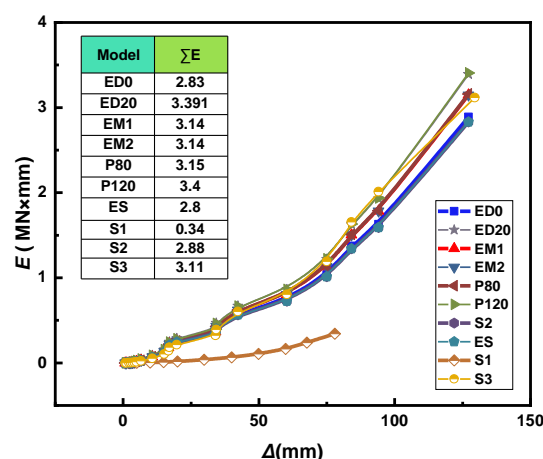
Figure 5. Prediction of energy dissipation in different concrete frames.

Table 4. Simulation test results of residual displacement rate for finite element specimens.

Specimen ID	Loading Displacement Angle and Residual Displacement Rate of Specimens (*R*)				
	$[\theta_e$ [1]] (1/550)	2 $[\theta_e]$ (1/275)	3 $[\theta_e]$ (1/183)	4 $[\theta_e]$ (1/138)	$[\theta_p$ [2]] (1/50)
S1	0.2	0.28	0.34	0.19	0.24
S2	0.17	0.27	0.29	0.18	0.22
S3	0.14	0.25	0.27	0.17	0.21
ES	0.17	0.29	0.35	0.19	0.24
P80	0.17	0.25	0.3	0.17	0.21
P120	0.12	0.22	0.31	0.19	0.2
ED0	0.15	0.25	0.29	0.17	0.2
ED20	0.17	0.27	0.31	0.18	0.21
EM1	0.13	0.25	0.3	0.12	0.19
EM2	0.13	0.25	0.3	0.12	0.19

[1] $[\theta_e]$ represents the limit of the interlayer displacement angle in the elastic state. [2] $[\theta_p]$ represents the limit of the interlayer displacement angle in the elasto-plastic state.

In summary, installing external self-centering devices after section enlargement significantly reduced the residual deformation of the reinforced frames under horizontal loads, while increasing the diameter of the energy-dissipating rebars or the strength of the rebars at the nodes had a minimal effect on the residual deformation. However, increasing prestress in prefabricated beams was effective in reducing residual deformation in the reinforced frames.

3. Dynamic Simulation Using OpenSees

To delve deeper into the effectiveness of this reinforcement method, OpenSees finite element analysis software was used for simulation studies. Initially, precise simulations

of the quasi-static tests on the three-frame structure were conducted to verify the validity and accuracy of the established numerical model. Subsequently, based on the structural characteristics of the actual reinforcement target (an existing building in Beijing), we constructed a detailed model of a four-story reinforced-concrete frame and applied the external self-resetting component reinforcement technology to enhance its seismic performance. Next, three representative earthquake waves were selected, and nonlinear time-history analyses were performed on the concrete frame models before and after reinforcement to assess the reinforcement effect.

3.1. Establishment of OpenSees Model

In modeling, the "Concrete02" model was used to simulate the constitutive relationship of concrete. Considering the reinforcing effect of stirrups and the degradation of the structural strength due to increased compressive strain made the simulation results more realistic. For the concrete cover, the "Concrete01" model, which did not consider the tensile strength, was chosen, to simplify calculations while still maintaining accuracy. The "Steel02" model was uniformly used for the constitutive relationships of the reinforcement and prestressed steel strands, accurately reflecting the isotropic strain-hardening characteristics of steel and ensuring the precise simulation of the material properties.

For element type selection, optimization was performed based on the component characteristics. Fiber elements were used for the detailed simulation of the beams and columns to capture their complex force characteristics. Truss elements were used for the prestressed steel strands and energy-dissipating reinforcements to enhance computational efficiency. Specifically, to accurately simulate the coordinated deformation between unbonded prestressed steel strands and the precast beams, the "Equal DOF" command was used to release the translational degrees of freedom of the steel strand nodes along the beam length, ensuring accuracy and reliability. For joint treatment, an "ENT" (Elastic—No Tension) material was used, effectively simulating the mechanical behavior of the joints under compression while neglecting their tensile capacity, thus reflecting the actual performance of the joints more realistically. Additionally, for columns at the joints, a rigid link beam was used to tightly connect the five nodes, forming a stable overall structure. The detailed division of the model elements and section settings is shown in Figure 6.
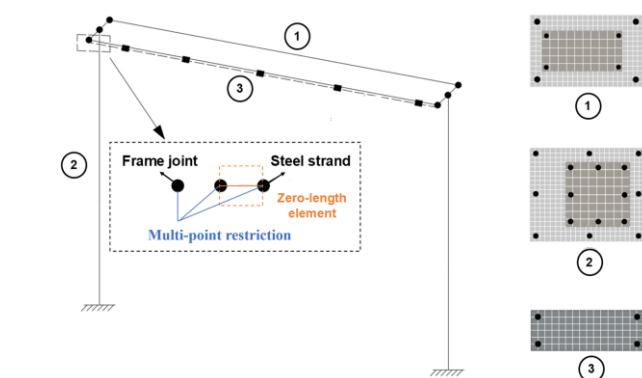
Figure 6. Unit division and section setting of the OpenSees model.

3.2. Quasi-Static Test Under OpenSees

The simulation results of the quasi-static tests on the LF1, LF2, and LF3 concrete frames are labeled as OpenSees-LF1, OpenSees-LF2, and OpenSees-LF3, respectively. Based on the actual test results of specimens LF1, LF2, and LF3, a comparative analysis of the hysteresis curves and backbone curves from static tests and OpenSees simulations was performed, and the results are shown in Figure 7. It is noteworthy that, during the actual static test of specimen LF1, a failure of the extensometer during reverse loading resulted in incomplete data collection for the negative direction of the hysteresis curve in the later stages of loading, causing some degree of data loss. Despite this, overall, the hysteresis

curves and backbone curves obtained from numerical simulations were in good agreement with the experimental data, with the error range controlled within 10%.

For the reinforced frames LF2 and LF3, the error between the numerical simulation results and the static test data was also strictly controlled to within 10%. This not only further verified the effectiveness of the seismic reinforcement method used, but also demonstrated the rationality and feasibility of the modeling approach and parameter settings employed in this study.

3.3. Nonlinear Time-History Analysis of the Structure

Based on the modeling method for reinforced frame structures in Section 3.1, finite element models of the existing reinforced-concrete frame structure (SL1) and its corresponding structure reinforced with self-resetting technology (SL2) were established in OpenSees. As shown in Figure 8a, the model represented a four-story reinforced-concrete frame building with a total height of 13,500 mm, a first-floor height of 3600 mm, and remaining floor heights of 3300 mm each. The structure was divided into three spans in the X-direction, each 6000 mm wide, and five spans in the Y-direction, each 5100 mm wide. For the reinforced SL2 structure, an additional self-resetting prefabricated beam reinforcement scheme was applied to the Y-direction façade; the finite element model is shown in Figure 8. The model was constructed using a three-dimensional, six-degree-of-freedom system, with the foundation completely fixed. Beams and columns were simulated using fiber models to accurately represent the material behaviors under complex loading conditions. The standard cube compressive strength of C20 concrete before reinforcement was 23.8 MPa; this was increased to 39.3 MPa for C40 concrete after reinforcement. The reinforcement, energy-dissipating reinforcement, and prestressed steel strands within the frame structure were simulated using "Steel02" material, with the HRB400 reinforcement having a yield strength of 400 MPa and the Q355 energy-dissipating reinforcement having a yield strength of 355 MPa. The prestressed steel strands were non-bonded with the concrete and were simulated using Truss elements, with a yield strength of 1680 MPa. The initial prestress of the steel strands in the prefabricated beams was 250 MPa, while the initial prestress of the cross-bracing was 450 MPa, with a diameter of 50 mm for the prestressed steel strands. This finite element model comprehensively reflected the geometric and material properties of the existing reinforced-concrete frame structure and was used to explore the significant effects of the self-resetting reinforcement technology on its performance improvements, providing theoretical and technical support for subsequent structural analysis and design optimization.

To verify the accuracy of the frame structure modeling, modal analysis was performed on the model built with the finite element software OpenSees, and the results were compared with the first three modes of the natural period modal analysis results from the YJK software (V4.3). The comparison of the results shown in Table 5 indicates that the calculation error between the two methods is within 15%, demonstrating the accuracy of the model and its suitability for subsequent time-history analysis.

Table 5. Comparison of the natural vibration periods of the previous three modes.

Specimen ID	Software	T1 (s)	T2 (s)	T3 (s)
SL1	YJK	1.159	1.143	1.015
	OpenSees	1.108	1.022	0.965
SL2	YJK	0.511	0.443	0.382
	OpenSees	0.521	0.422	0.394
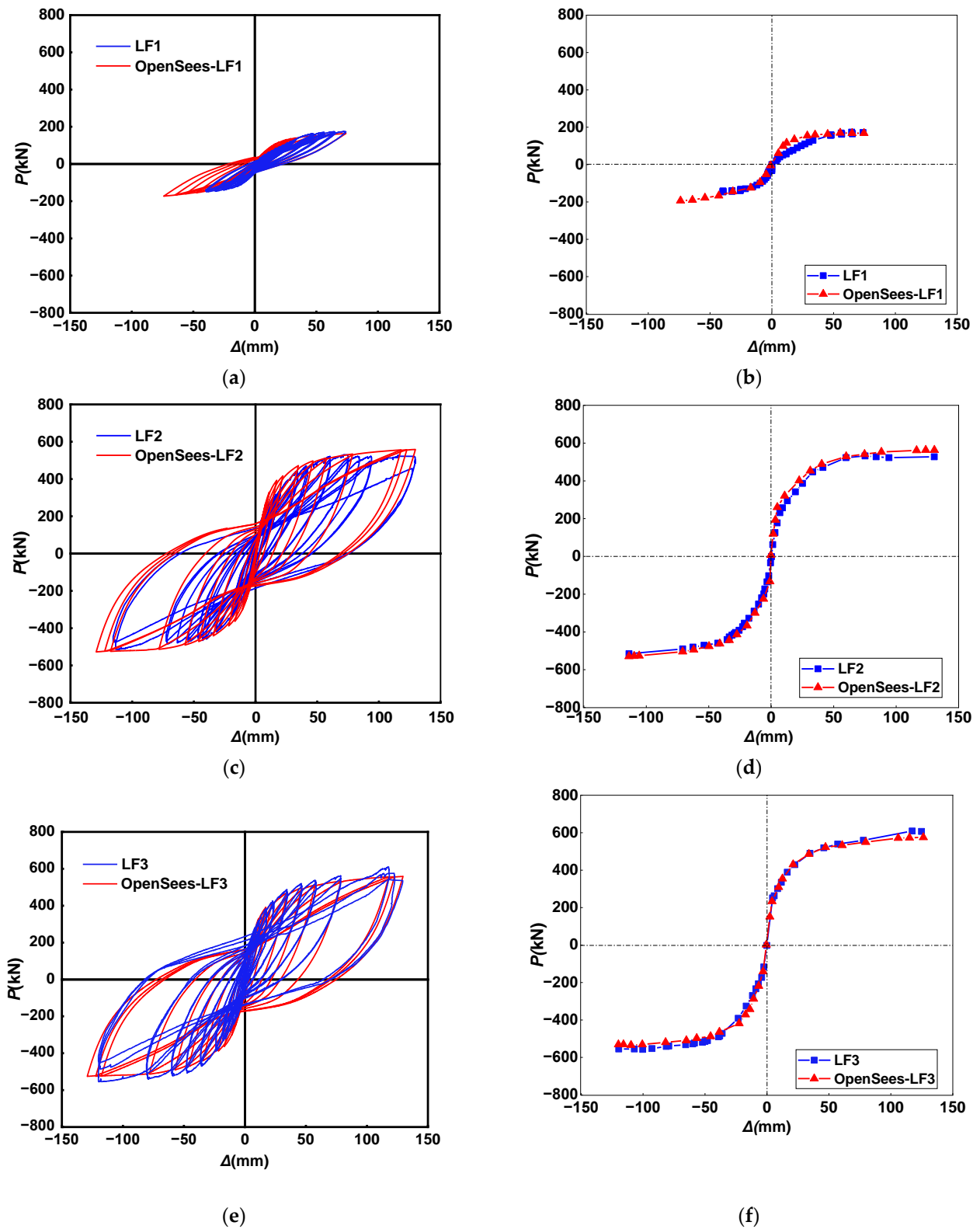
Figure 7. Hysteresis curve and skeleton curve of quasi-static test and OpenSees simulation. (**a**) Fitting of the horizontal load–displacement curve for LF1 in OpenSees. (**b**) Fitting of the skeleton curve for LF1 in OpenSees. (**c**) Fitting of the horizontal load–displacement curve for LF2 in OpenSees. (**d**) Fitting of the skeleton curve for LF2 in OpenSees. (**e**) Fitting of the horizontal load–displacement curve for LF3 in OpenSees. (**f**) Fitting of the skeleton curve for LF3 in OpenSees.
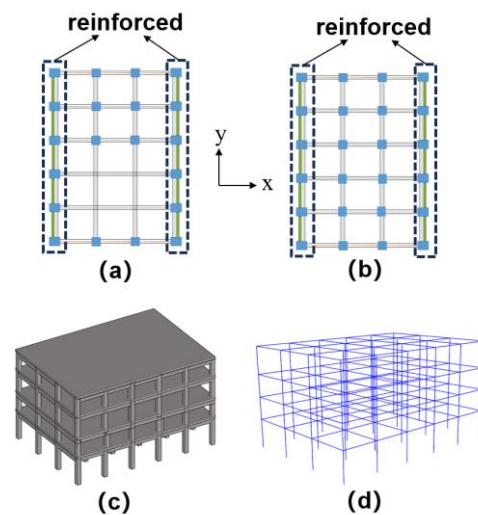
Figure 8. OpenSees finite element full-scale model. (**a**) First-floor plan of the framework model. (**b**) Other-floor plan of the framework model. (**c**) Three-dimensional schematic diagram of frame model. (**d**) OpenSees framework model.

The site category of the existing reinforced-concrete frame structure in this project was Category II, with a site characteristic period T_g of 0.4 s. Therefore, for the analysis, two natural earthquake waves and one artificial earthquake wave were selected based on the site characteristic period: the Chi-Chi-Taiwan wave, the Cape Mendocino wave, and an artificial wave. Detailed information on these three waves is provided in Table 6 and Figure 9. Subsequently, response spectrum analysis was conducted for the three earthquake waves and compared with the standard response spectrum for an area with a seismic fortification level of 8 degrees. As shown in Figure 10, the error between the response spectra of the earthquake waves and the standard spectrum was within 20%. Then, the peak ground accelerations of the three earthquake waves were scaled to 70 gal, 200 gal, and 400 gal to calculate the seismic response of the frame structure in the Y-direction under 8-degree, frequently occurring, design-basis, and rarely occurring earthquakes.

Table 6. Simulation test results of residual displacement rate for finite element specimens.

Earthquake	Station	Date	PGA (G)	Duration (S)	Record Gap
Chi-Chi-Taiwan	TCU065	1999	2.33	28.96	0.02
Cape Mendocino	Petrolia	1992	1.89	30.2	0.02
Artificial	—	—	1.00	38.95	0.02
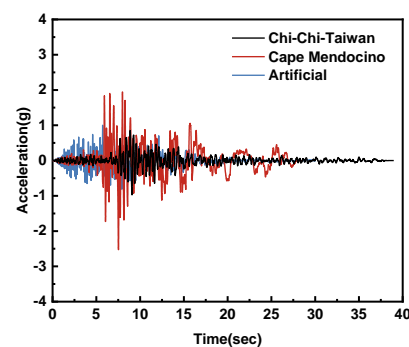
Figure 9. Seismic waveform.
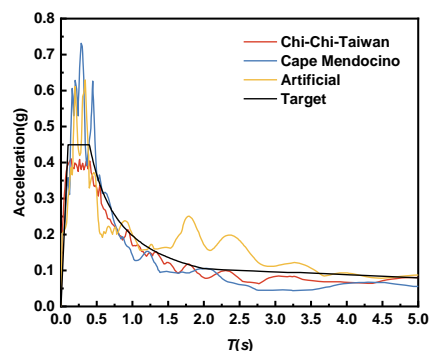
Figure 10. Reaction spectrum analysis.

Figure 11 shows the top floor displacement time-history curves in the Y-direction for the unreinforced frame SL1 and the reinforced frame SL2 under the influence of three different earthquake waves. It can be observed that, for the top-floor measurement points, the impact of the peak ground acceleration was more significant, between 5 and 15 s of the earthquake motion input. The maximum floor displacement and peak-to-peak distance at the top of frame SL2 were significantly reduced to a maximum of 66.6% compared to those of the unreinforced frame SL1, and the oscillation amplitude of the time-history curve was smaller, indicating that the self-resetting seismic reinforcement method effectively improved the seismic performance of the structure, increased its lateral stiffness, and shortened its natural period. Furthermore, the reinforcement effect became more pronounced with the increased seismic loading.

Figure 12 shows the comparison of the maximum floor displacement curves for each floor, before and after the structural reinforcement, under the influence of the three different earthquake waves. The maximum floor displacement for each level of the reinforced SL2 frame was less than that of the unreinforced SL1 frame. In the unreinforced SL1 frame, the displacement was primarily concentrated on the first floor under seismic action whereas, in the SL2 frame, the maximum floor displacement was more uniformly distributed, with a nearly linear increase with height. The maximum floor displacement on the first floor was significantly reduced, with no notable inter-story displacement concentration observed. As the seismic action intensified, the maximum inter-story displacement angle of the frame structure significantly increased. Under the influence of the three earthquake waves in the Y-direction, the SL1 frame structure did not meet the seismic performance level-3 requirements of the "Code for Seismic Design of Buildings" [6] and it even exceeded the plastic displacement angle limit of 1/50 during rare earthquakes, with one floor exhibiting a sudden change in the inter-story displacement angle, indicating a risk. The SL2 frame structure in the Y-direction met the seismic performance level-3 requirements (with inter-story deformations less than the elastic displacement limit of 1/550 under frequent earthquakes, slightly exceeding the elastic limit of 1/550 under design-basis earthquakes, and less than twice the elastic displacement limit of 1/275 under rare earthquakes), indicating that the reinforced frame structure with the two self-resetting seismic reinforcement methods exhibited good seismic resilience.

The residual displacement primarily reflects a structure's self-recovery capability after an earthquake. The comparison of the residual displacements between the reinforced and unreinforced frames under different earthquake waves is shown in Figure 13. As the earthquake intensity increased, the residual displacement of the reinforced frame decreased significantly and followed a linear relationship. The residual displacements of the reinforced frame were significantly reduced compared to those of the unreinforced frame, with reductions of up to 61.6, 62.8, and 65.4% in the Y-direction for frequent, design-basis, and rare earthquakes, respectively. The Cape Mendocino wave had a significant effect on the overall deformation of the structure. The maximum displacement of the unreinforced frame under Y-direction horizontal seismic action was 10.414 mm while, for the reinforced frame under the same conditions, the maximum displacement was only 3.668 mm, result-

ing in a reduction of about 64.7%. Additionally, under frequent earthquakes, the residual displacement of the reinforced frame decreased by approximately 55.82 to 60.44% and, under design-basis earthquakes, it decreased by about 62.78 to 63.22%. This result indicates that using external self-resetting components for reinforcement can effectively reduce residual displacement. Furthermore, the reduction in the residual displacement became more pronounced as the seismic intensity increased, which is of importance for improving the seismic performances of old concrete frame structures that lack self-resetting capabilities.
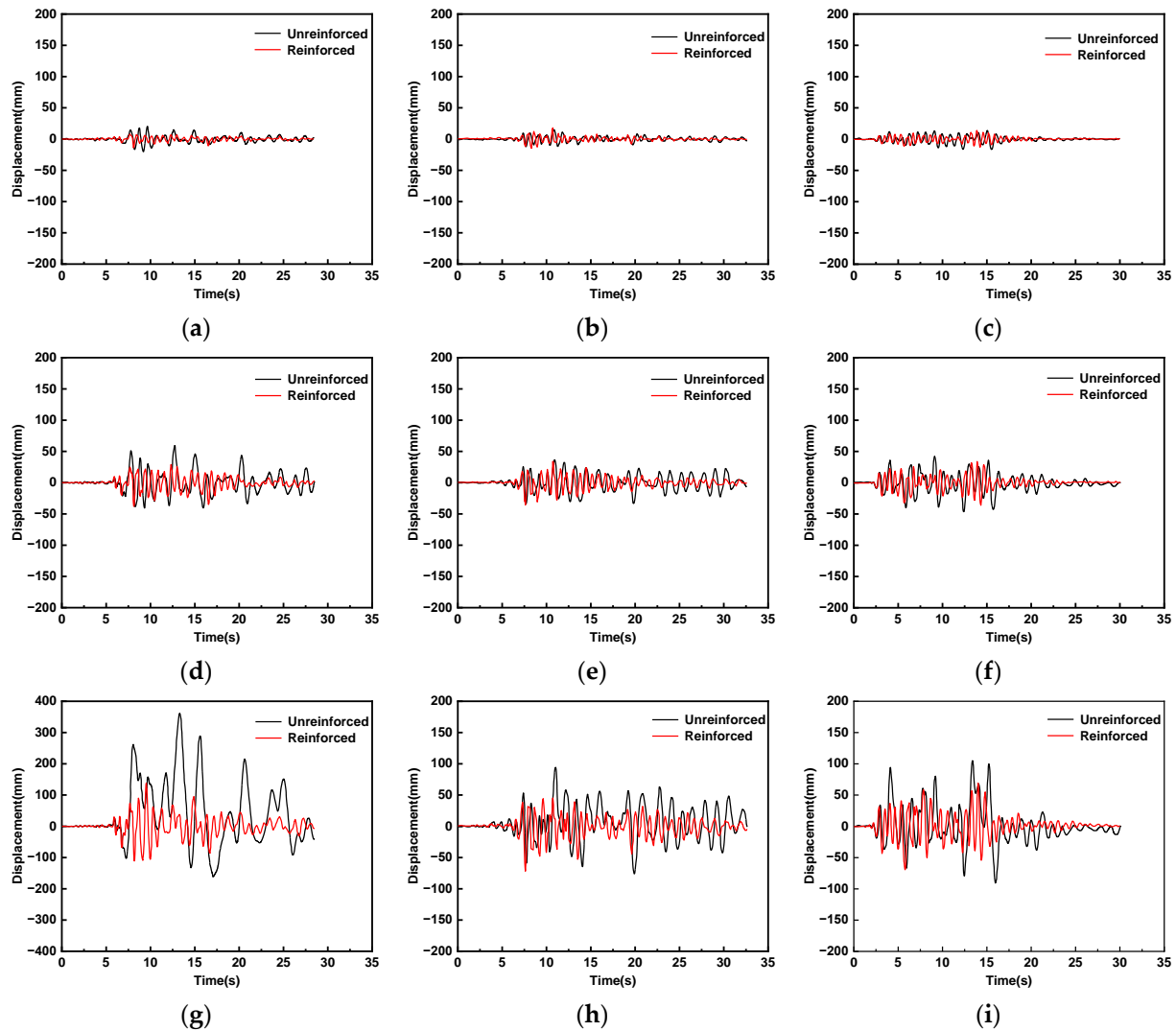
Figure 11. Comparison of displacement time-history curves before and after reinforcement. (**a**) Frequently occurring earthquake: Chi-Chi-Taiwan. (**b**) Frequently occurring earthquake: Cape Mendocino. (**c**) Frequently occurring earthquake: artificial. (**d**) Design-basis earthquake: Chi-Chi-Taiwan. (**e**) Design-basis earthquake: Cape Mendocino. (**f**) Design-basis earthquake: artificial. (**g**) Rarely occurring earthquake: Chi-Chi-Taiwan. (**h**) Rarely occurring earthquake: Cape Mendocino. (**i**) Rarely occurring earthquake: artificial.
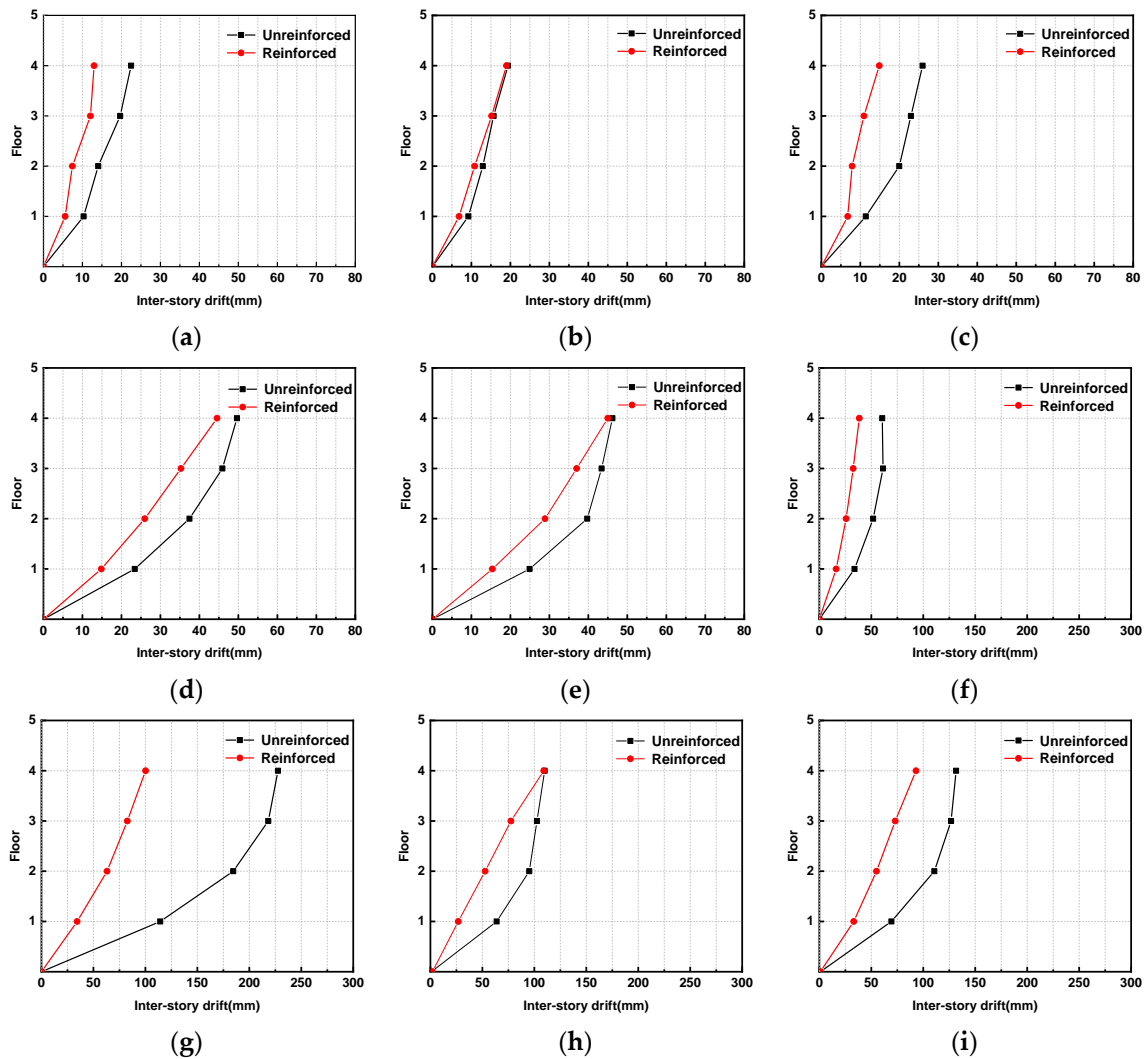
Figure 12. Maximum displacement curve of each floor before and after structural reinforcement. (**a**) Frequently occurring earthquake: Chi-Chi-Taiwan. (**b**) Frequently occurring earthquake: Cape Mendocino. (**c**) Frequently occurring earthquake: artificial. (**d**) Design-basis earthquake: Chi-Chi-Taiwan. (**e**) Design-basis earthquake: Cape Mendocino. (**f**) Design-basis earthquake: artificial. (**g**) Rarely occurring earthquake: Chi-Chi-Taiwan. (**h**) Rarely occurring earthquake: Cape Mendocino. (**i**) Rarely occurring earthquake: artificial.
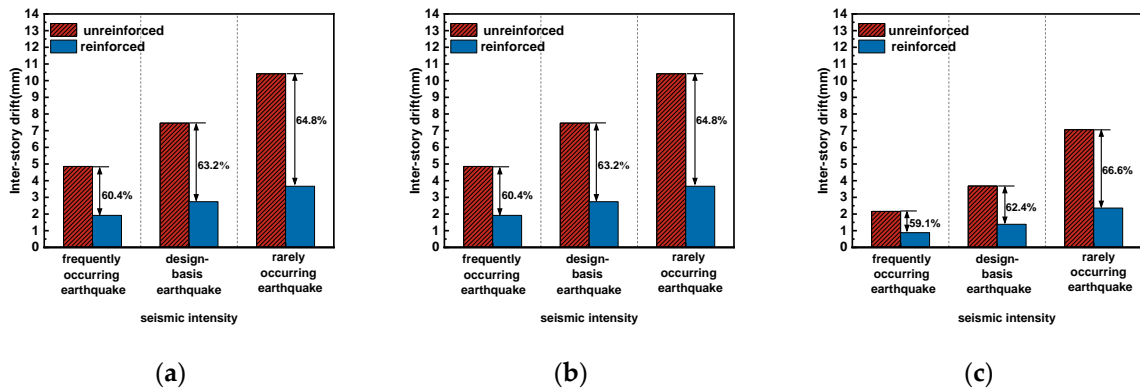
Figure 13. Comparison of residual displacements before and after structural reinforcement: (**a**) Chi-Chi-Taiwan, (**b**) Cape Mendocino, and (**c**) artificial wave.

4. Conclusions

In this study, two types of finite element simulation software were used to further study the self-resetting component reinforcement method based on static test data for modeling validation. ABAQUS was used for reinforcement simulations of a single frame, adjusting the frame component parameters to study the factors affecting the seismic performance after reinforcement. OpenSees was used for the dynamic simulation of the reinforced building. The following main findings were obtained:

(1) For the static simulation of a single frame before and after reinforcement, the modeling results from ABAQUS and OpenSees had an experimental error of less than 10%.

(2) Analysis using the ABAQUS software revealed that the main factor affecting the reinforcement effect was the prestressed tendons inside the prefabricated beams. By increasing the tensile force of the prestressed steel strands, the residual deformation rate of the reinforced frame can be reduced by 26%.

(3) Analysis using the OpenSees software showed that, compared to non-reinforced buildings, reinforced buildings exhibit better seismic characteristics when subjected to three types of earthquake waves, with the residual displacement reduced by 55.82–64.7%.

(4) As the peak ground acceleration increased, the reduction in the residual deformation of the reinforced building became more pronounced and exhibited a linear relationship.

Supplementary Materials: The following supporting information can be downloaded at: https://www.mdpi.com/article/10.3390/buildings14113666/s1, Figure S1: The reinforcement method and seismic mechanism of a frame system strengthened by external self-centering components; Figure S2: The static test loading protocol; Figure S3: Finite element model of the frame before reinforcement; Figure S4: Reinforcement framework of the finite element model of the frame before reinforcement; Figure S5: Mesh of the finite element model of the frame before reinforcement; Figure S6: Finite element model of a frame system strengthened by external self-centering com-ponents; Figure S7: Reinforcement framework of the finite element model of a frame system strengthened by external self-centering components; Figure S8: Mesh of the finite element model of a frame system strengthened by external self-centering components; Figure S9: Interaction settings of the finite element model of a frame system strengthened by ex-ternal self-centering components. (a) Energy-dissipating reinforcement conduit contact. (b) Unbonded prestressing tendon spring. (c) Slip interface at the end of the precast beam. (d) Tensioning end constraint of the prestressing tendon.

Author Contributions: Methodology, H.L.; software, Y.F. and J.S.; writing—original draft preparation, Y.F.; writing—review and editing, Y.F. and X.Z.; supervision, Y.F. All authors have read and agreed to the published version of the manuscript.

Data Availability Statement: The original contributions presented in the study are included in the article and Supplementary Materials, further inquiries can be directed to the corresponding author.

Conflicts of Interest: Author Hang Liu was employed by Beijing Building Construction Research Institute Co., Ltd. The remaining authors declare that the research was conducted in the absence of any commercial or financial relationships that could be construed as a potential conflict of interest.

References

1. Das, T.K.; Choudhury, S. Developments in the unified performance-based seismic design. *J. Build. Pathol. Rehabil.* **2023**, *8*, 13. [CrossRef]
2. Padalu, P.K.V.R.; Surana, M. An overview of performance-based seismic design framework for reinforced concrete frame buildings. *Iran. J. Sci. Technol. Trans. Civ. Eng.* **2024**, *48*, 635–667. [CrossRef]
3. Patel Vasudev, T. Ajay Radke Performance-based seismic design of reinforced concrete structure—A review. *Int. Res. J. Adv. Eng. Hub. IRJAEH* **2024**, *2*, 555–558. [CrossRef]
4. Zameeruddin, M.; Sangle, K.K. Review on recent developments in the performance-based seismic design of reinforced concrete structures. *Structures* **2016**, *6*, 119–133. [CrossRef]
5. Zeng, B.; Li, Y. Towards performance-based design of masonry buildings: Literature review. *Buildings* **2023**, *13*, 1534. [CrossRef]
6. *GB50011-2010*; Code for Seismic Design of Buildings. Standardization Administration of China: Beijing, China, 2016.

7. Li, Y.Y.; Guo, B.; Liu, J. Research on reinforced concrete beam enlarged cross section method experiment and finite element simulation. *Appl. Mech. Mater.* **2014**, *638–640*, 208–213. [CrossRef]

8. Prakash, A.; Agarwala, S.K.; Singh, K.K. Optimum design of reinforced concrete sections. *Comput. Struct.* **1988**, *30*, 1009–1011. [CrossRef]

9. Wang, Y.D.; Yang, S.; Han, M.; Yang, X. Experimental study of section enlargement with reinforced concrete to increase shear capacity for damaged reinforced concrete beams. *Appl. Mech. Mater.* **2012**, *256–259*, 1148–1153. [CrossRef]

10. Cao, J.; Du, J.; Fan, Q.; Yang, J.; Bao, C.; Liu, Y. Reinforcement for earthquake-damaged glued-laminated timber knee-braced frames with self-tapping screws and CFRP fabric. *Eng. Struct.* **2024**, *306*, 117787. [CrossRef]

11. Naser, M.Z.; Hawileh, R.A.; Abdalla, J. Modeling strategies of finite element simulation of reinforced concrete beams strengthened with FRP: A review. *J. Compos. Sci.* **2021**, *5*, 19. [CrossRef]

12. Pan, B.; Liu, F.; Zhuge, Y.; Zeng, J.-J.; Liao, J. ECCs/UHPFRCCs with and without FRP reinforcement for structural strengthening/repairing: A state-of-the-art review. *Constr. Build. Mater.* **2022**, *316*, 125824. [CrossRef]

13. Rafieizonooz, M.; Kim, J.-H.J.; Varaee, H.; Nam, Y.; Khankhaje, E. Testing methods and design specifications for FRP-prestressed concrete members: A review of current practices and case studies. *J. Build. Eng.* **2023**, *73*, 106723. [CrossRef]

14. Raza, A.; Khan, Q.U.Z.; Ahmad, A. Numerical investigation of load-carrying capacity of GFRP-reinforced rectangular concrete members using CDP model in ABAQUS. *Adv. Civ. Eng.* **2019**, *2019*, 1745341. [CrossRef]

15. Reichenbach, S.; Preinstorfer, P.; Hammerl, M.; Kromoser, B. A review on embedded fibre-reinforced polymer reinforcement in structural concrete in europe. *Constr. Build. Mater.* **2021**, *307*, 124946. [CrossRef]

16. Wei, J.; Ying, H.; Yang, Y.; Zhang, W.; Yuan, H.; Zhou, J. Seismic performance of concrete-filled steel tubular composite columns with ultra high performance concrete plates. *Eng. Struct.* **2023**, *278*, 115500. [CrossRef]

17. El-Emam, M.M.; Bathurst, R.J. Influence of reinforcement parameters on the seismic response of reduced-scale reinforced soil retaining walls. *Geotext. Geomembr.* **2007**, *25*, 33–49. [CrossRef]

18. Maheri, M.R.; Sahebi, A. Use of steel bracing in reinforced concrete frames. *Eng. Struct.* **1997**, *19*, 1018–1024. [CrossRef]

19. Huang, H.; Chen, Z.; Zhao, M.; Wang, B.; Ye, Y. Seismic performance of frame with middle partially encased composite brace and steel-hollow core partially encased composite spliced frame beam. *J. Build. Eng.* **2024**, *95*, 110226. [CrossRef]

20. Anilkumar, P.M.; Haldar, A.; Scheffler, S.; Rao, B.N.; Rolfes, R. Numerical studies on the design of self-resetting active bistable cross-shaped structure for morphing applications. *Proceedings* **2020**, *64*, 16. [CrossRef]

21. Chancellor, N.; Eatherton, M.; Roke, D.; Akbaş, T. Self-centering seismic lateral force resisting systems: High performance structures for the city of tomorrow. *Buildings* **2014**, *4*, 520–548. [CrossRef]

22. Guo, M.; Shen, Y. Research on the influence of mild steel dampers on seismic performance of self-resetting pier. *Staveb. Obz.-Civ. Eng. J.* **2021**, *30*, 105–118. [CrossRef]

23. Zhang, Q.; Xiong, E. Research Progress of Self-Centering Structure System. In Proceedings of the 2021 7th International Conference on Hydraulic and Civil Engineering & Smart Water Conservancy and Intelligent Disaster Reduction Forum (ICHCE & SWIDR), Nanjing, China, 6–8 November 2021; IEEE: New York, NY, USA, 2021; pp. 406–410.

24. Zhong, C.; Christopoulos, C. Self-centering seismic-resistant structures: Historical overview and state-of-the-art. *Earthq. Spectra* **2022**, *38*, 1321–1356. [CrossRef]

25. Huang, H.; Li, M.; Zhang, W.; Yuan, Y. Seismic behavior of a friction-type artificial plastic hinge for the precast beam–column connection. *Arch. Civ. Mech. Eng.* **2022**, *22*, 201. [CrossRef]

26. Huang, H.; Li, M.; Yuan, Y.; Bai, H. Experimental Research on the Seismic Performance of Precast Concrete Frame with Replaceable Artificial Controllable Plastic Hinges. *J. Struct. Eng.* **2023**, *149*, 4022222. [CrossRef]

27. Aure, T.W.; Ioannides, A.M. Simulation of crack propagation in concrete beams with cohesive elements in ABAQUS. *Transp. Res. Rec. J. Transp. Res. Board* **2010**, *2154*, 12–21. [CrossRef]

28. Cao, X.; Wu, L.; Li, Z. Behaviour of steel-reinforced concrete columns under combined torsion based on ABAQUS FEA. *Eng. Struct.* **2020**, *209*, 109980. [CrossRef]

29. Lee, S.-H.; Abolmaali, A.; Shin, K.-J.; Lee, H.-D. ABAQUS modeling for post-tensioned reinforced concrete beams. *J. Build. Eng.* **2020**, *30*, 101273. [CrossRef]

30. Mohammad Noh, N.; Liberatore, L.; Mollaioli, F.; Tesfamariam, S. Modelling of masonry infilled RC frames subjected to cyclic loads: State of the art review and modelling with OpenSees. *Eng. Struct.* **2017**, *150*, 599–621. [CrossRef]

31. Qingfu, L.; Wei, G.; Yihang, K. Parameter calculation and verification of concrete plastic damage model of ABAQUS. *IOP Conf. Ser. Mater. Sci. Eng.* **2020**, *794*, 012036. [CrossRef]

32. Baltzopoulos, G.; Baraschino, R.; Iervolino, I.; Vamvatsikos, D. Dynamic analysis of single-degree-of-freedom systems (DYANAS): A graphical user interface for OpenSees. *Eng. Struct.* **2018**, *177*, 395–408. [CrossRef]

33. Kechidi, S.; Colaço, A.; Alves Costa, P.; Castro, J.M.; Marques, M. Modelling of soil-structure interaction in OpenSees: A practical approach for performance-based seismic design. *Structures* **2021**, *30*, 75–88. [CrossRef]

34. Lu, X.; Xie, L.; Guan, H.; Huang, Y.; Lu, X. A shear wall element for nonlinear seismic analysis of super-tall buildings using OpenSees. *Finite Elem. Anal. Des.* **2015**, *98*, 14–25. [CrossRef]

35. McKenna, F. OpenSees: A framework for earthquake engineering simulation. *Comput. Sci. Eng.* **2011**, *13*, 58–66. [CrossRef]

36. Feng, S.; Yang, Y.; Xue, Y.; Yu, Y. Numerical Investigation on the Hysteretic Performance of Self-Centering Precast Steel–Concrete Hybrid Frame. *Buildings* **2024**, *14*, 3202. [CrossRef]
37. Yu, S.; Zhang, Y.; Bie, J.; Zhang, W.; Jiang, J.; Chen, H.; Chen, X. Finite Element Analysis of Hysteretic Behavior of Superposed Shear Walls Based on OpenSEES. *Buildings* **2023**, *13*, 1382. [CrossRef]